Development and assessment of atomistic models for predicting static friction coefficients

Soran Jahangiri, Gavin S. Heverly-Coulson, and Nicholas J. Mosey*
Department of Chemistry, Queen's University, Kingston, Canada, K7L 3N6
(Received 27 October 2015; revised manuscript received 17 May 2016; published 4 August 2016)

The friction coefficient relates friction forces to normal loads and plays a key role in fundamental and applied areas of science and technology. Despite its importance, the relationship between the friction coefficient and the properties of the materials forming a sliding contact is poorly understood. We illustrate how simple relationships regarding the changes in energy that occur during slip can be used to develop a quantitative model relating the friction coefficient to atomic-level features of the contact. The slip event is considered as an activated process and the load dependence of the slip energy barrier is approximated with a Taylor series expansion of the corresponding energies with respect to load. The resulting expression for the load-dependent slip energy barrier is incorporated in the Prandtl-Tomlinson (PT) model and a shear-based model to obtain expressions for friction coefficient. The results indicate that the shear-based model reproduces the static friction coefficients μ_s obtained from first-principles molecular dynamics simulations more accurately than the PT model. The ability of the model to provide atomistic explanations for differences in μ_s amongst different contacts is also illustrated. As a whole, the model is able to account for fundamental atomic-level features of μ_s, explain the differences in μ_s for different materials based on their properties, and might be also used in guiding the development of contacts with desired values of μ_s.

DOI: 10.1103/PhysRevB.94.075406

I. INTRODUCTION

Friction is a force resisting the relative movement of objects in contact and plays an important role in the efficiency and functionality of many devices. From the standpoint of efficiency, a significant portion of the world's energy is consumed by friction, which has deleterious economic and environmental effects [1–3]. Numerous studies have been undertaken to develop a better fundamental understanding of the factors that influence friction and to guide efforts to control friction [4–11]. These studies show that while friction manifests as a macroscopic phenomenon, it is influenced by atomic-level details such as the alignment of structural features of the surfaces in contact [12,13], the strengths of interactions between atoms on these surfaces [14], changes in bonding during slip [15], atomic-level surface roughness [16], surface vibrational frequencies [17], and mechanical resonances of the sliding system [18].

The Prandtl-Tomlinson (PT) model [19,20] is often used to connect friction forces measured experimentally to microscopic properties of sliding contacts [21–26]. In this model, the slip event between two objects is considered as an activated process through a transition state connecting two equilibrium structures. The energy barrier to the slip process is reduced by the mechanical work performed on the system due to the application of a tangential force F, which increases the rate at which slip occurs. The PT model predicts dependencies of friction on temperature T and sliding velocity v that are consistent with experiments [27–32] and molecular simulations [33–36].

Experimental observations indicate that the friction force F_f generally obeys Amontons's law [37] $F_f = \mu L$, where L is a load applied normal to the slip interface and μ is a constant called the friction coefficient. Although μ is a key parameter in many applications, its atomic-level origins remain poorly understood [22]. Models describing the $F_f - L$ relationship based on macroscopic properties and contact mechanics can in principle be used to predict μ [38–40]. However, the absence of a model connecting μ to the atomic-level features of contacts impedes the elucidation of many fundamental aspects of friction and the rational design of contacts with desired μ. Such abilities are important, for instance, in the design of nanoelectromechanical and microelectromechanical systems [41,42] and solid lubricants [43,44].

The goal of this study is to develop a model that accurately relates μ to atomic-level features of sliding contacts that can be measured experimentally or predicted through calculations. For this purpose, we explore the load dependence of F_f predicted by the PT model and show that the resulting expression for μ is unable to account for the contribution of adhesive interactions between sliding surfaces in μ. Accordingly, we develop an alternative expression for the $F_f - L$ relationship and use this expression to obtain a model which relates μ to energetic, structural, and mechanical properties of a contact. The model is based on the assumption that slip occurs when the energy of a sheared interface reaches the slip barrier. The abilities of both models to reproduce and shed light on the origins of different values of μ are examined with respect to first-principles molecular dynamics (FPMD) simulations for a set of ionic (MgO), covalent (Si and Ge), and lamellar [MoS_2, WS_2, graphite, graphane, fluorographane (FG), hydrofluorographane (HFG), and boron nitride (BN)] materials. The results demonstrate that the model developed here consistently reproduces the FPMD simulation results. Furthermore, the model accounts for the differences in μ amongst these systems on the basis of their energetic, structural, and mechanical properties, offers insights into the origin of μ, and provides the basis for designing contacts with desired values of μ.

*moseyn@queensu.ca

The remainder of this paper is organized as follows. The models for μ are presented in Sec. II. The computational methods and model systems are described in Sec. III. The results of the simulations are described and compared with predictions of the models in Sec. IV. Conclusions are reported in Sec. V.

II. MODEL DEVELOPMENT

The models developed in this work consider the slip event as an activated process in which the system is transformed from one equilibrium structure, the reactants (R), to another equilibrium structure, the products (P), through a transition state (TS) structure. A representative example of this process, which is conceptually analogous to the PT model, is shown for the MgO [110](110) slip system in Fig. 1. This slip event involves the translation of the system along a slip path with a corresponding change in energy E. While the energy barrier to the slip process ΔE_{slip} can in principle be overcome thermally, slip is typically induced via the application of a force F applied along the slip direction. The application of F deforms R toward the TS and the mechanical energy put into the system reduces the thermal barrier associated with the slip event. For low values of F, the system shears uniformly as illustrated by the middle structure in Fig. 1. At some point, F will exceed F_f and the system will slip by moving past TS to P, shown as the rightmost structure in Fig. 1. Analogous processes occur for the other interfaces investigated in this work.

According to Amontons's law, μ describes the L dependence of F_f. Since F_f depends on the energetic barrier to slip, in what follows we first develop an expression for approximating the changes in ΔE_{slip} with L in Sec. II A. The resultant expression for ΔE_{slip} is then used in conjunction with the definition of F_f obtained from the PT model to develop a model for μ in Sec. II B. Section II C outlines an alternative to the PT model that is based on the shear energy of the system and ΔE_{slip}.

The development of the models is based on the assumption that the system of interest can be contained within a cell defined by the lattice vectors **a**, **b**, and **c**. Furthermore, it is assumed that the cell is oriented such that **a** is always aligned with the x axis, **b** always resides in the x-y plane, and **c** is defined by three components c_x, c_y, and c_z. This assumption allows the cell to be defined by the vector $\mathbf{h}^T = (a_x, b_y, c_x, c_y, c_x, b_x)$.

A. Load-dependent slip barrier

The energy barrier of the slip process ΔE_{slip} is the difference in the internal energies of TS and R, E_{TS} and E_{R}, respectively, plus the work performed against L due to the change in the thickness of the system $\Delta h_3(L)$ that occurs upon moving from R to TS [45]:

$$\Delta E_{\text{slip}} = E_{\text{TS}}(L) - E_{\text{R}}(L) + L\Delta h_3(L). \tag{1}$$

The L-dependent internal energies of R and TS can be approximated by second-order Taylor series expansions of the energies of these structures with respect to changes in **h** about their respective $L = 0$ structures. For example, the internal energy of R can be expressed as

$$E_{\text{R}}\left(\mathbf{h}_{\text{R}}^0 + \delta\mathbf{h}_{\text{R}}\right) = E_{\text{R}}\left(\mathbf{h}_{\text{R}}^0\right) + \tfrac{1}{2}\delta\mathbf{h}_{\text{R}}^T\mathbf{C}_{\text{R}}\delta\mathbf{h}_{\text{R}}, \tag{2}$$

where $\mathbf{h}_{\text{R}}^0$ designates the lattice vectors of R when $L = 0$, $\delta\mathbf{h}_{\text{R}}$ is a deformation vector whose components quantify the L-induced changes in the lattice vectors, the first-order term in the Taylor series is zero because all first derivatives of E_{R} with respect to changes in **h** are zero, and $\mathbf{C}_{\text{R}}$ is the stiffness matrix, whose components correspond to second derivatives of E_{R} with respect to all combinations of the components of **h**.

The application of L corresponds to subjecting the cell to a force vector **F**, whose only nonzero component is of magnitude L and aligned with h_3. Assuming the system behaves elastically, the force and deformation vectors are related as

$$\delta\mathbf{h} = \mathbf{C}^{-1}\mathbf{F}, \tag{3}$$

and in the case where L is the only nonzero component of **F**, one obtains

$$\delta\mathbf{h}^T\mathbf{C}\delta\mathbf{h} = \chi_{33}^0 L^2, \tag{4}$$

where $\chi_{33}^0 = \mathbf{C}_{33}^{-1}$ is obtained by inverting the stiffness matrix.

The work term in Eq. (1) can be expressed as

$$L\Delta h_3(L) = L\left[h_{3,\text{TS}}^0 - h_{3,\text{R}}^0\right] + L[\delta h_{3,\text{TS}} - \delta h_{3,\text{R}}], \tag{5}$$

where $h_{3,\text{TS}}^0$ and $h_{3,\text{R}}^0$ are the thicknesses of the TS and R structures in the absence of L, and $\delta h_{3,\text{TS}}$ and $\delta h_{3,\text{R}}$ are the changes in the thicknesses of these structures due to the application of L. Equation (3) allows the change in the

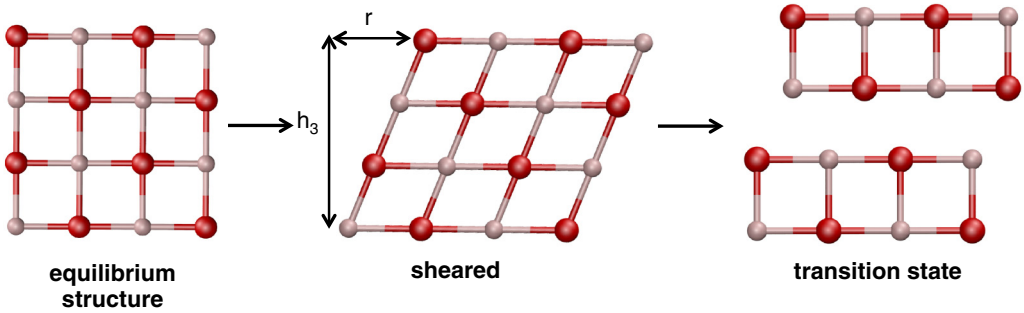

FIG. 1. Structures observed during an FPMD simulation of MgO undergoing slip along the [110](110) slip direction. The leftmost image illustrates the equilibrium structure of MgO. The central image shows MgO subjected to a shear deformation that has caused the top of the system to move a distance r along the slip direction. The rightmost image shows the TS for this slip event. The symbol h_3 designates the thickness of the system. Red and pink spheres indicate oxygen and Mg atoms, respectively.

thickness to be expressed as

$$\delta h_3 = -\chi^0_{33} L, \tag{6}$$

where the negative sign appears in this equation because a sign convention has been adopted in which a positive L tends to decrease the thickness of the system.

Inserting Eqs. (2), (4), and (5) into Eq. (1) yields the load-dependent slip barrier

$$\Delta E_{\text{slip}}(L) = \Delta E^0_{\text{slip}} + \Delta h^0_3 L - \frac{\Delta \chi^0_{33}}{2} L^2, \tag{7}$$

where ΔE^0_{slip} is the value of ΔE_{slip} in the absence of L, $\Delta h^0_3 = h^0_{3,TS} - h^0_{3,R}$ is the change in the thickness of the system upon moving from R to TS in the absence of L, and $\Delta \chi^0_{33}$ is the difference between the values of the (3,3) components of the compliance matrices of the TS and R when $L = 0$.

B. Prandtl-Tomlinson model

The PT model is widely used to provide atomic-level insights into friction. In this model, a point mass [24] (or masses) [46,47] is connected to a spring and dragged along a surface with a periodic potential, which leads to predicted friction forces of [29,32,48]

$$F_f = F_s - \left[\beta k_B T \ln\left(\frac{v_c}{v}\right)\right]^{2/3}, \tag{8}$$

where F_s is the maximum force at which slip occurs spontaneously [21], T is the temperature of the system, k_B is Boltzmann's constant, and v is the sliding velocity. The parameter $v_c = (2 f_0 \beta k_B T)/(3 C_{\text{eff}} \sqrt{F_s})$, where f_0 is the frequency at which the system attempts to move past the TS, and C_{eff} represents the stiffness of the contact. β is a parameter that is dependent upon the shape of the surface potential. For the commonly used case of a sinusoidal surface potential [29,30]

$$E(r) = -\frac{\Delta E_{\text{slip}}}{2} \cos\left(\frac{2\pi r}{a}\right), \tag{9}$$

$\beta = (3\pi\sqrt{F_s})/(2\sqrt{2}a)$, where a is the periodicity of the potential. F_s is also related to the shape of the surface potential, being associated with the slope of the potential at an inflection point between R and TS. In the case of the sinusoidal potential in Eq. (9), F_s is given by [29,32]

$$F_s = \frac{\pi \Delta E_{\text{slip}}}{a}. \tag{10}$$

The PT model indicates that F_f can be described in terms of F_s and corrections for thermal and velocity effects. Differentiating Eq. (8) with respect to a load L, acting normal to the interface provides the friction coefficient μ:

$$\mu = \mu_s \left\{1 - \left[\beta_0 \ln\left(\frac{v_0}{v}\right)\right]^{2/3}\right\}, \tag{11}$$

where $\mu_s = dF_s/dL$, $\beta_0 = (3\pi k_B T)/(2\sqrt{6} a F_s)$, $v_0 = (f_0 k_B T \pi)/(\sqrt{2} a C_{\text{eff}})$, and a, f_0, and C_{eff} have been treated as load-independent parameters. Equation (11) indicates that μ can be described in terms of the constant μ_s, with corrections for thermal and velocity effects. The decrease in μ with T and the logarithmic dependence upon v predicted in this model have been observed experimentally in studies in diverse fields [49–57].

Equation (11) indicates that μ_s is a key contributor to the overall friction coefficient. An expression for this parameter can be obtained by inserting the L-dependent expression for ΔE_{slip} in Eq. (7) into the definition of F_s in Eq. (10) and differentiating the result with respect to L:

$$\mu_s = \frac{\pi}{a}\left(\Delta h^0_3 - \Delta \chi^0_{33} L\right) \xrightarrow{L \to 0} \frac{\pi \Delta h^0_3}{a}. \tag{12}$$

The $L = 0$ limit of Eq. (12), which is most useful for practical applications occurring at low loads, only accounts for the changes in F_s required to provide the system with enough mechanical energy to overcome the L-dependent portion of the slip barrier arising from changes in the thickness that occur as the system progresses from R to TS in the presence of L. However, Eq. (12) neglects changes in F_s arising from L-dependent changes in the curvature of the surface potential and ΔE_{slip}, which include potentially important contributions from changes in the interactions between the surfaces forming the interface during slip. The inability of Eq. (12) to account for these L-dependent changes will limit the general utility of this model. This is supported by the results of the calculations reported in Sec. IV B, which show that Eq. (12) does not accurately reproduce values of μ_s predicted through FPMD simulations of a variety of systems.

The deficiencies of Eq. (12) are ultimately due to the use of a sinusoidal surface potential. Indeed, the periodic nature of such a potential leads to the cancellation of terms that incorporate the L dependence of the interactions between the sliding surfaces and curvature of the potential. The PT model can be used in conjunction with other surface potentials [25,34] and extended to include interactions between multiple contacts [46,47,58], which may lead to alternative definitions of μ_s; however, such potentials are not general in nature, but instead can only be used in conjunction with systems having surface potentials that vary in specific ways and lead to more complex expressions for F_f and μ. In what follows, we develop a more general approach for describing the changes in energy that occur during a slip process to develop a general model definition of μ_s.

C. Shear-based model

As illustrated in Fig. 1, subjecting a material to F causes it to deform. If the deformation is described as a shear, the energy as a function of r can be expressed as [59]

$$E_{\text{shear}}(r, L) = \frac{G + G' L}{2} r^2, \tag{13}$$

where G is the stiffness of the system along the slip direction and G' is the first derivative of G with respect to L. G can be obtained by calculating the second derivative of E_R with respect to r and G' can be obtained by differentiating G with respect to changes in L. The force applied along the slip direction at a given L and r can be obtained by differentiating Eq. (13) with respect to r:

$$F(r, L) = (G + G' L) r. \tag{14}$$

The quadratic shear potential contained in Eq. (13) does not contain an inflection point, which would be associated with F_s. Instead, within this model slip occurs spontaneously when $E_{\text{shear}}(L) = \Delta E_{\text{slip}}(L)$. This approximation might be expected to cause an overestimation of the actual value of F_s. However, as illustrated in Sec. IV B, this model leads to values of F_s and μ_s that are in good agreement with values obtained through FPMD simulations of the same systems.

Assuming that slip becomes spontaneous when $E_{\text{shear}}(L) = \Delta E_{\text{slip}}(L)$, using Eq. (13) to represent $E_{\text{shear}}(L)$ and Eq. (7) to represent $\Delta E_{\text{slip}}(L)$ leads to a value of r at which slip occurs spontaneously:

$$r_s(L) = \sqrt{\frac{2\Delta E_{\text{slip}}(L)}{G + G'L}}. \tag{15}$$

Evaluating Eq. (14) at this point and expanding the result in conjunction with the expression for $\Delta E_{\text{slip}}(L)$ presented in Eq. (7) yields

$$F_s = [t_0 + t_1 L + t_2 L^2 + t_3 L^3]^{1/2}, \tag{16a}$$

$$t_0 = 2G\Delta E^0_{\text{slip}}, \tag{16b}$$

$$t_1 = 2\left(G\Delta h^0_3 + G'\Delta E^0_{\text{slip}}\right), \tag{16c}$$

$$t_2 = 2\left(G'\Delta h^0_3 - \frac{G\Delta\chi^0_{33}}{2}\right), \tag{16d}$$

$$t_3 = -\frac{GG'\chi^0_{33}}{2}. \tag{16e}$$

Following an approach analogous to the manner in which Eq. (8) is obtained within the PT model [21], the shear-based model leads to

$$F_f = \left[F_s^2 - 2(G + G'L)k_BT\ln\left(\frac{v_0}{v}\right)\right]^{1/2}, \tag{17}$$

where $v_0 = k_BTf_0/F_s$. Differentiating both sides of this equation with respect to L yields

$$\mu = \frac{F_s}{F_f}\mu_s - \frac{k_BT}{F_f}\left[G'\ln\left(\frac{v_0}{v}\right) - \frac{(G + G'L)\mu_s}{F_s}\right], \tag{18}$$

where $\mu_s = dF_s/dL$. In the limit where $T = 0$ K, the last term on the right-hand side of Eq. (18) becomes zero and $F_f = F_s$, which yields

$$\mu = \mu_s = \frac{t_1 + 2t_2L + 3t_3L^2}{2F_s}. \tag{19}$$

In the $L = 0$ limit, μ becomes

$$\mu_s(0) = \frac{G'r^0_s}{2} + \frac{\Delta h^0_3}{r^0_s}, \tag{20}$$

where $r^0_s = \sqrt{2\Delta E^0_{\text{slip}}/G}$ is the value of r_s when $L = 0$.

The first term on the right-hand side of Eq. (20) accounts for the change in the curvature of E_{shear} when the system is subjected to L. The second term on the right-hand side of Eq. (20) is analogous to the PT expression for μ_s [Eq. (12)] and accounts for the increase in F_s that is required to provide the system with sufficient energy to perform the work required to undergo a change in thickness upon moving from R to TS in the presence of L. In addition, the influence of adhesive interactions on μ_s is incorporated through the appearance of r_s in both terms. The inclusion of L-dependent changes in the adhesive interactions across the slip interface in the shear-based model and the absence of these effects in the PT model accounts for the main difference between the underlying physics captured by these models.

III. MODEL SYSTEMS AND COMPUTATIONAL DETAILS

The abilities of the models described in Sec. II to provide accurate values of $\Delta E_{\text{slip}}(L)$ and low-T values of F_f and μ, F_s and μ_s, respectively, were assessed through a combination of static density functional theory (DFT) calculations and first-principles molecular dynamics (FPMD) simulations. The static DFT calculations were performed to obtain values for the parameters entering the models described above, while the FPMD simulations were used as a reference for evaluating the accuracy of the PT and shear-based models. The systems on which the calculations were performed and the details of the calculations are discussed in this section.

It is noted that the effects of T and v on μ can be assessed by using Eqs. (11) and (18). However, obtaining reference values of these quantities computationally requires extensive simulations at various temperatures, low-velocity regimes, and on large system sizes, which are beyond the reach of FPMD simulations. Accordingly, we leave such investigations for a future work in which empirical force fields and rate enhancement simulation approaches such as parallel replica dynamics [60,61] will be employed. Instead, we focus on examining the abilities of these models to reproduce F_s and μ_s, which are important parameters in the definitions of F_f and μ that can be examined through FPMD simulations at low T.

A. Model systems

The materials investigated in this work represent systems that undergo slip via changes in ionic (MgO), covalent (Si and Ge), and nonbonding interactions (graphite, BN, MoS_2, WS_2, graphane, FG, and HFG). The typical structures of these materials are shown in Figs. 1 and 2 and the corresponding slip directions are outlined in Table I. The abilities of the PT and shear-based models to predict the friction forces and coefficients for these materials were assessed with respect to the results of FPMD simulations.

TABLE I. Number of atoms per unit cell n_{atom}, slip system, k-point grids, and s_6 values for the systems examined in this study.

Material	n_{atom}	Slip system	k-point grid	s_6
MgO	8	[110](110)	$3 \times 3 \times 3$	0.75
Si	6	[110](111)	$4 \times 4 \times 2$	0.75
Ge	6	[110](111)	$5 \times 5 \times 2$	0.75
MoS_2	6	$[21\bar{3}0](0001)$	$3 \times 3 \times 1$	0.65
WS_2	6	$[21\bar{3}0](0001)$	$3 \times 3 \times 1$	0.65
BN	4	$[21\bar{3}0](0001)$	$4 \times 4 \times 2$	0.41
Graphite	4	$[21\bar{3}0](0001)$	$4 \times 4 \times 2$	0.61
Graphane	8	$[21\bar{3}0](0001)$	$3 \times 3 \times 1$	0.75
FG	8	$[21\bar{3}0](0001)$	$4 \times 4 \times 1$	0.75
HFG	8	$[21\bar{3}0](0001)$	$4 \times 4 \times 1$	0.75

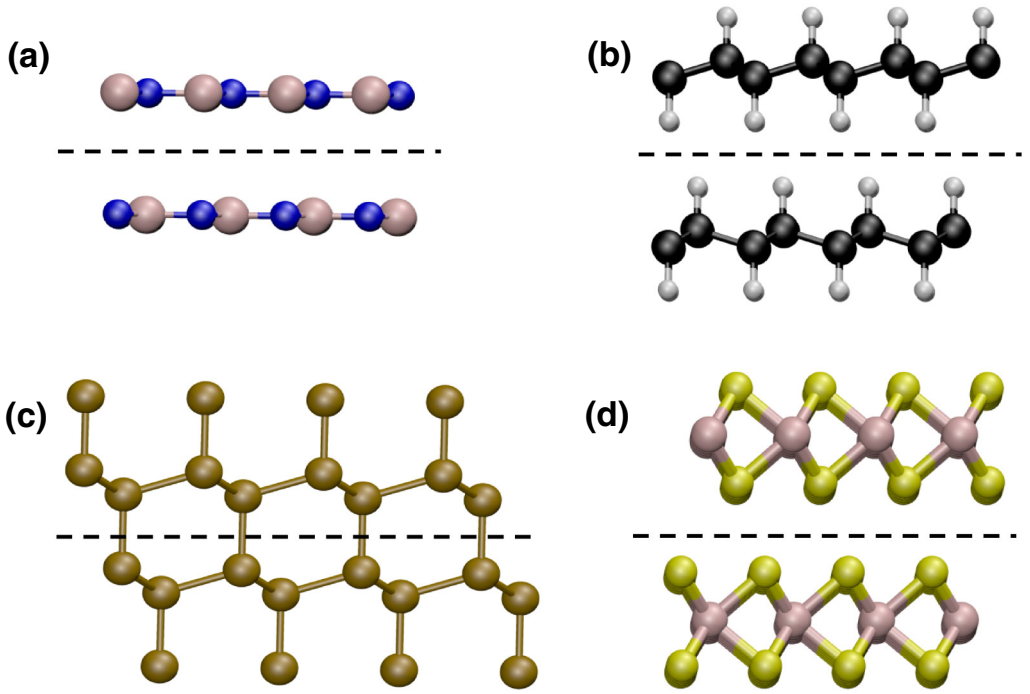

FIG. 2. Structures of the systems considered in this work. In all cases, the dashed line designates the slip plane and slip occurs by the atoms above the slip plane moving rightward relative to those beneath the slip plane. (a) BN and graphite. In BN, the sheets contain alternating B (pink) and N (blue) atoms. In graphite, the system consists entirely of carbon. (b) Graphane, FG, and HFG. In all cases, black spheres indicate carbon atoms. In graphane, the white spheres indicate hydrogen atoms, while they indicate fluorine atoms in FG. In HFG, the white spheres below each layer of carbon atoms represent hydrogen atoms, while those above each layer of carbon atoms correspond to fluorine atoms. (c) Si and Ge. The brown spheres indicate Si or Ge atoms as appropriate. (d) MoS_2 and WS_2. The yellow spheres indicate sulfur atoms and the pink spheres indicate Mo or W as appropriate.

B. Computational details

The static DFT [65,66] calculations for all systems were performed using the exchange-correlation functional of Perdew, Burke, and Ernzerhof [67] plus corrections for dispersion interactions (PBE + D) [68,69]. In all cases, the valence electrons were represented by a set of plane waves expanded to a kinetic energy cutoff of 45 Ry, the core electrons were represented by projector augmented potentials [70], and integration of the Brillouin zone was performed using the k-point grids specified in Table I. The s_6 parameter used to scale the contributions of the dispersion interactions to the energy was adjusted to closely reproduce experimental interlayer spacings of the lamellar materials in cases where experimental values for these spacings were available. In all other cases, this parameter was set to 0.75 [68]. The full set of s_6 values is included in Table I. Overall, this methodology was found to closely reproduce the experimental lattice parameters of the materials examined in this study, with the data in Table II showing the experimental and calculated values agree to within 2% or better in all cases where experimental data were available, with most calculated lattice parameters agreeing to within better than 1% of the experimental values.

The stress-free R and TS structures were located for all systems with the generalized solid-state nudged elastic band (GSS-NEB) method [71], which we added to the QUANTUM ESPRESSO simulation package [72]. The GSS-NEB method locates the minimum energy path (MEP) connecting the R and P structures for the slip process using a series of structures between R and P. The differences in the structures along the MEP account for the movement of the atoms and lattice vectors during the slip process. The highest energy point on the path is allowed to move along the MEP to locate the TS structure. The differences in the energies of TS and R were used to determine ΔE_{slip} and the structures of R and TS were used to determine Δh_3^0 and a.

The stiffness matrices $\mathbf{C}$ of R and TS were obtained by evaluating numerical second derivatives of the energies of these structures with respect to small changes in their zero-L lattice vectors. The resulting stiffness matrices were inverted to obtain compliance matrices for R and TS, and used to obtain $\Delta\chi_{33}^0$. The stiffness along the slip direction G was obtained by evaluating numerical second derivatives of the energy of R with respect to small changes in r. G' was obtained by numerically differentiating G with respect to L.

The FPMD simulations were performed using the same electronic structure methods described above. This ensures that a consistent potential is used to determine the parameters used in the model and to obtain the friction forces and coefficients in the FPMD simulations, which were used to assess the models. The dynamics was performed using a time step of 1.0 fs, which conserved total energy to better than 1.0×10^{-5} au/ps in simulations performed in the NVE ensemble. In all simulations, the systems were oriented such that the slip plane was aligned with the **a** and **b** lattice vectors, which also spanned the x-y plane. L was applied normal to the slip plane and the system was

TABLE II. Comparison of experimental and calculated lattice vector lengths for the bulk unit cells of the systems examined in this study. Note that experimental values were not available for all lattice vectors of graphane, FG, and HFG.

Material	Lattice vector	DFT value (Å)	Expt. value (Å)
MgO	**a**	2.119	2.106[a]
Si	**a**	3.884	3.840[a]
Ge	**a**	4.003	4.000[a]
MoS_2	**a**	3.176	3.160[a]
	c	12.298	12.295[a]
WS_2	**a**	3.202	3.18[a]
	c	12.494	12.5[a]
BN	**a**	2.509	2.504[a]
	c	6.639	6.661[a]
Graphite	**a**	2.461	2.456[a]
	c	6.674	6.696[a]
Graphane	**a**	2.529	2.42[b]
	c	8.719	NA
FG	**a**	2.609	2.57[c]
	c	11.494	NA
HFG	**a**	2.569	NA
	c	9.554	NA

[a]Values from Ref. [62].
[b]Values from Ref. [63].
[c]Values from Ref. [64].

equilibrated at $T = 100$ K while allowing the cell to move according to the method of Parrinello and Rahman [73] to maintain the desired L. The low T used in the simulations permits the prediction of F_s and μ_s because Eqs. (8), (11), (17), and (18) indicate that $F_f \approx F_s$ and $\mu \approx \mu_s$ in this regime. After equilibration, the systems were sheared by altering the x and y components of the **c** lattice vector such that the top of the simulation cell moved along the slip direction at a rate of 1.0 Å/ps using Lees-Edwards boundary conditions [74]. In addition, the **a** and **b** lattice vectors as well as the z component of the **c** lattice vector were allowed to move according to the method of Parrinello and Rahman to maintain the desired value of L along the direction normal to the slip plane and zero stresses along all other directions. The constant kinetic energy cutoff approach of Bernasconi *et al.* [75] was used to maintain a consistent basis set as the cell changed shape and size during these simulations. The stresses acting along the slip direction were taken from the internal stress tensor obtained during the simulations, with the maximum shear stress along the slip direction τ_c observed during the simulation used to define $F_s = \tau_c A$. All calculations were performed using the QUANTUM ESPRESSO software package [72] that we modified to permit the application of time-dependent stresses and strains.

IV. RESULTS AND DISCUSSION

The models described in Sec. II provide means of estimating the load dependency of the slip energy barriers, shear energies, and friction forces which are then used to provide models for estimating the friction coefficients. In this section, the accuracies of these models are assessed by comparing the predicted energies, forces, and friction coefficients against values obtained through quantum chemistry calculations and FPMD simulations. In Sec. IV A, the slip barriers given by Eq. (7) and deformation energies given by Eqs. (9) and (13) are compared against values obtained through GSS-NEB calculations. The values of F_s and μ_s predicted by the PT and shear models are compared with the results of FPMD simulations in Sec. IV B. Furthermore, the shear-based model is used to rationalize the differences in μ_s obtained for the systems considered in this study in Sec. IV C and a brief mathematical analysis on the structure of this model is discussed in Sec. IV D. The parameters entering the models were calculated as described in Sec. III and are summarized in Table III.

A. Assessment of the energy models

The slip energy barriers ΔE_{slip} predicted from Eq. (7) are compared against GSS-NEB calculations in Fig. 3(a). The barriers were calculated with normal stresses ranging from 0 to 5 GPa, in 1-GPa intervals, for all the materials along the slip

TABLE III. Values of ΔE^0_{slip}, a, Δh^0_3, G, G', and $\Delta \chi^0_{33}$ obtained through static DFT calculations and used as parameters in the PT and shear models for the systems examined in this study.

Material	ΔE^0_{slip} (kJ mol^{-1})	a (Å)	Δh^0_3 (Å)	G (nN Å^{-1})	G' (Å^{-1})	$\Delta \chi^0_{33}$ (Å nN^{-1})
MgO	207.80	2.997	6.23×10^{-1}	5.79×10^{0}	8.34×10^{-2}	5.66×10^{-2}
Si	99.37	3.846	-2.95×10^{-2}	6.48×10^{-1}	6.10×10^{-2}	8.01×10^{-2}
Ge	72.33	4.000	2.97×10^{-1}	6.50×10^{-1}	1.68×10^{-1}	1.19×10^{-1}
MoS_2	1.44	1.536	6.95×10^{-2}	5.80×10^{-2}	2.07×10^{-1}	-2.78×10^{-3}
WS_2	1.65	2.006	1.15×10^{-1}	8.00×10^{-2}	2.65×10^{-1}	1.25×10^{-2}
BN	0.33	1.455	1.63×10^{-2}	3.70×10^{-2}	9.59×10^{-2}	-1.83×10^{-1}
Graphite	0.33	1.422	1.78×10^{-2}	2.80×10^{-2}	1.12×10^{-1}	-8.91×10^{-2}
Graphane	0.62	1.510	3.91×10^{-2}	5.00×10^{-2}	4.33×10^{-1}	-2.80×10^{-3}
FG	0.28	1.509	4.54×10^{-2}	4.20×10^{-2}	6.14×10^{-2}	-1.28×10^{-3}
HFG	1.43	1.519	5.60×10^{-2}	1.05×10^{-1}	8.94×10^{-2}	-2.69×10^{-3}

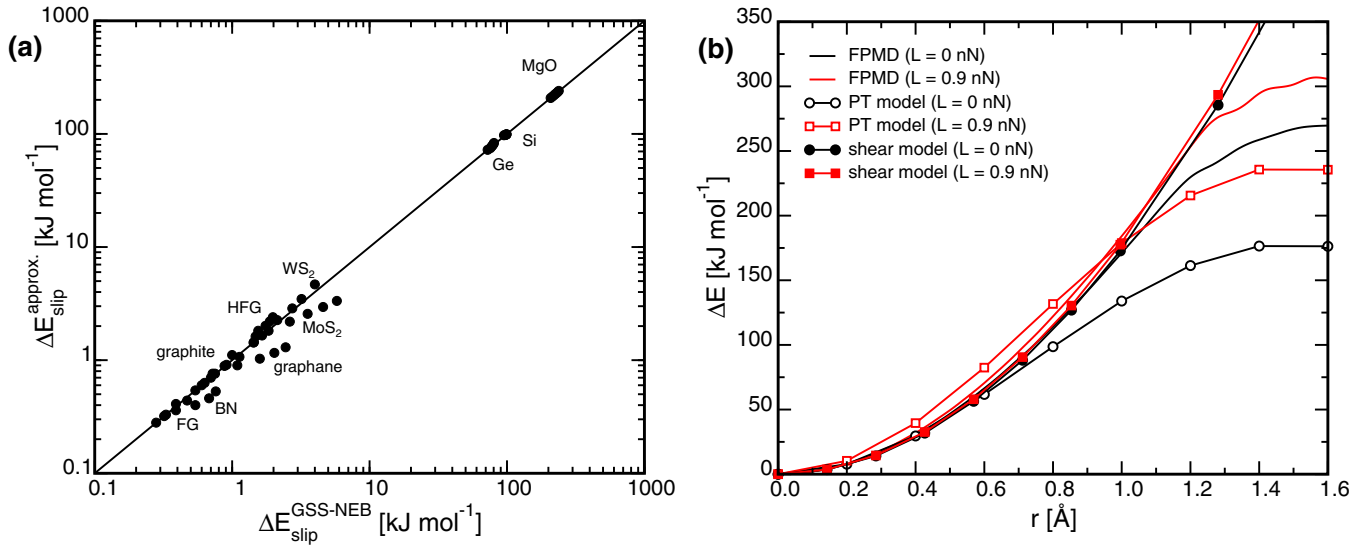

FIG. 3. (a) Comparison of values of ΔE_{slip} obtained with Eq. (7), $\Delta E_{\text{slip}}^{\text{approx}}$, and GSS-NEB calculations, $\Delta E_{\text{slip}}^{\text{GSS-NEB}}$. (b) Comparison of the deformation energies ΔE of MgO as a function of shear distance r obtained with FPMD simulations, the shear model [Eq. (13)], and the PT model with a sinusoidal potential [Eq. (9)], at loads of 0 and 0.9 nN.

systems outlined in Table I. There is a good agreement between the ΔE_{slip} values obtained with the two methods, with all predicted values lying very close to the diagonal line indicating a perfect correlation. From a quantitative perspective, the average absolute difference (AAD) and the maximum absolute difference (MAD) between the predicted values and the GSS-NEB barriers are 0.5 and 2.7 kJ mol^{-1}, respectively. As expected for a model based on a truncated Taylor series expansion, the deviations between the predicted and GSS-NEB barriers increase with L. Nonetheless, the differences are comparable to, or even lower than, experimental errors [30] of about 8 kJ mol^{-1} and thus suitable for the ultimate purpose of approximating μ_s.

The deformation energies obtained from the PT model [Eq. (9)] and the shear-based model [Eq. (13)] for shearing MgO moving along the [110](110) slip direction at loads of 1 and 5 GPa are plotted against analogous quantities obtained through FPMD simulations in Fig. 3(b). The data show that the energies obtained with the shear model and FPMD simulations agree well for $r < \sim 0.6$ Å when $L = 0$ nN, and $r < \sim 1.0$ Å when $L = 0$ nN, with deviation occurring when the FPMD energies reach an inflection point at which slip is initiated. Meanwhile, the PT energies deviate from the FPMD results at much lower values of r for both loads considered, with the PT results diverging from the FPMD energies before the latter reach the inflection point at which slip starts. Overall, these results indicate that the shear model outperforms the PT model in terms of accounting for the changes in the energy of MgO prior to slip. Similar results were obtained for other systems in this study. However, it should be noted that despite the agreement between the FPMD simulations and the shear-based model in Fig. 3(b), the use of truncated Taylor series expansions in Eqs. (13) and (7) may limit the abilities of the model to predict μ_s quantitatively for contacts that undergo significant deviations from elastic behavior when subjected to shear and compressive stresses.

B. Friction forces and coefficients

The abilities of the shear and PT models to predict F_s and μ_s were assessed by comparing the values obtained with these models against the results of FPMD simulations. The changes in F for the MgO[110](110) slip system obtained through these three approaches are shown in Fig. 4(a). These data show that F increases in a roughly linear manner during the FPMD simulations to reach a maximum value, which can be associated with F_s, before dropping rapidly as slip occurs. The shear model reproduces this behavior, with that model leading to a linear increase in F followed by an instantaneous drop in F to zero when $r = r_s$ is reached. The data in this figure also show that value of r_s predicted with the shear model is similar to the r at which slip occurred in the FPMD simulation, and that the values of F_s obtained with the shear model are similar to the FPMD values. By contrast, the PT data do not agree well with the FPMD results. Specifically, the shape of the PT $F - r$ curve differs significantly from that obtained through the FPMD simulations, the PT model reaches F_s at much lower values of r than the FPMD simulations, and the resulting values of F_s significantly underestimate the FPMD values of this quantity.

The data in Fig. 4(a) suggest that the shear model outperforms the PT model in terms of predicting F_s. To explore this further, the values of F_s predicted with both PT [Eq. (10)] and shear [Eq. (16)] models for all systems are compared with the results of the FPMD simulations in Fig. 4(b). It should be noted that the parameters in Table III were used to obtain the values of F_s at several loads for both models and the FPMD results were obtained by averaging the maximum forces sustained before

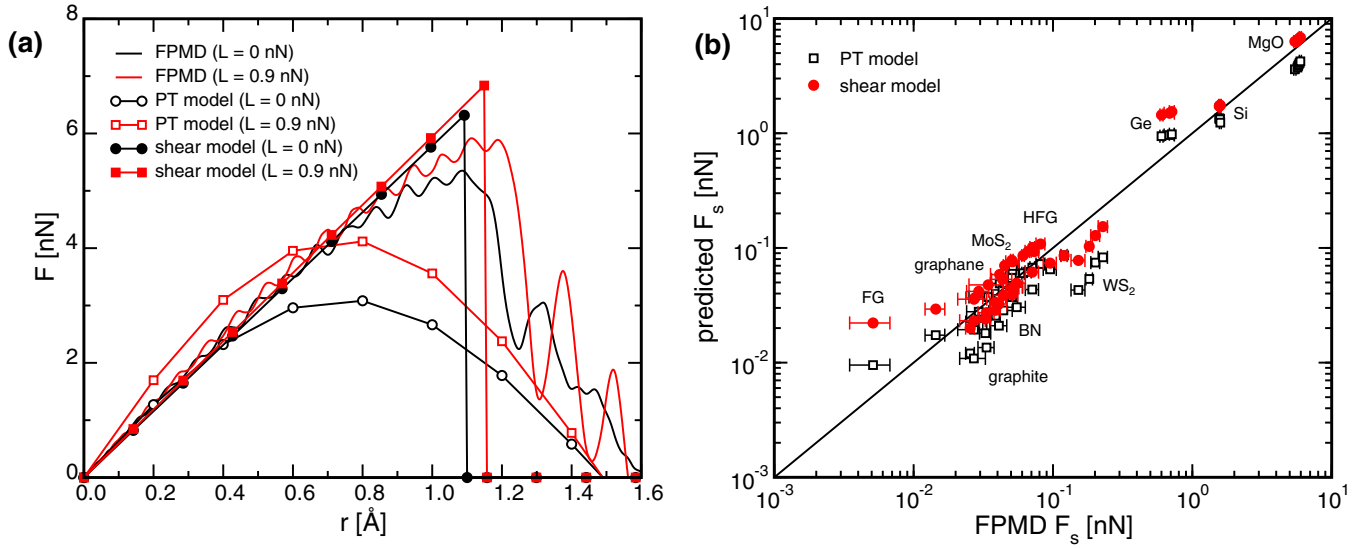

FIG. 4. (a) Applied force F versus shear distance r for the MgO [110](110) slip system obtained with FPMD simulations, the PT model, and the shear model at loads of 0 and 0.9 nN. (b) Friction forces F_s obtained with the shear and PT models compared against corresponding values obtained through FPMD simulations. Horizontal error bars represent standard deviation in quantities obtained through five independent FPMD simulations, and vertical error bars indicate standard deviations on the slopes obtained through linear least-squares fits to the F_s values predicted by the shear and PT models over the same values of L used in the FPMD simulations.

slip in five independent FPMD simulations performed at each load. The data in Fig. 4(b) indicate a good agreement between the values of F_s obtained with both the shear and PT models against the results of the FPMD simulations. However, the shear model performs slightly better with an AAD of 0.17 nN and an MAD of 0.88 nN with respect to the FPMD data. The corresponding values of the PT model are 0.27 and 1.95 nN, respectively. It should be noted that the differences between the predicted and FPMD values are systematic for a given system and the resulting values of μ_s, which depend on the change in F_s with L, are still in a reasonable agreement with the reference data.

The values of μ_s were obtained through linear least-squares fits of the values of F_s obtained at different loads with the shear and PT models and the FPMD simulations. The resulting values are plotted in Fig. 5. The results obtained from the shear model have an AAD of 0.016 and MAD of 0.054 with respect to the FPMD simulations, whereas the analogous errors for the PT models are 0.058 and 0.128, respectively. Furthermore, the PT model yields some completely erroneous results, such as predicting a negative μ_s (-0.041) for Si (the point is not included in the plot due to the logarithmic scale). Overall, results in Fig. 5 clearly indicate that the shear model outperforms the PT model in terms of evaluating μ_s. The inability of the PT model to accurately predict μ_s is due to the lack of contributions from the changes in the shape of the potential and height of the potential with L, as noted in Sec. II B. These results indicate that the shear model (or a modified PT model) should be used in cases where G' is sufficiently large to cause the first term in Eq. (20), which accounts for L-dependent changes in the potential and barrier, to be comparable in magnitude, or even larger than, the second term in that equation.

C. Application to materials

In this section, the shear-based model will be used to rationalize the difference in the values of μ_s obtained for the systems considered in this study in terms of the parameters entering Eq. (20). Since this model outperforms the PT model

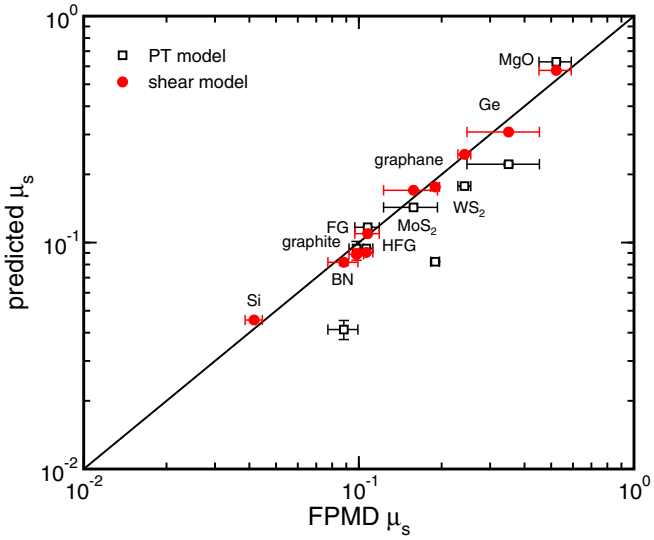

FIG. 5. Friction coefficients μ_s obtained with the shear and PT models compared against corresponding values obtained through FPMD simulations. Horizontal error bars represent standard deviation in quantities obtained through five independent FPMD simulations, and vertical error bars indicate standard deviations on the slopes obtained through linear least-squares fits to the F_s values predicted by the shear and PT models over the same values of L used in the FPMD simulations.

in predicting the values of μ_s, emphasis will be placed on the shear-based model. In addition, the following analysis will focus on the $L = 0$ limit of the shear-based model for μ_s because this expression is most relevant to applications occurring at low L and lends itself to straightforward analysis. The general form of the shear-based definition of μ_s is examined in greater detail in Sec. IV D.

The results in Fig. 5 show that MgO has the highest μ_s of all materials considered in this study. Given that this material is ionically bonded, one may assume that the high value of μ_s is due to the large slip barrier of 207.81 kJ mol^{-1}. While the large slip barrier leads to a large F_s, analysis of the terms entering Eq. (20) in conjunction with the parameters in Table III shows that change in the thickness of the system upon moving from R to TS is the main contributor to μ_s for MgO. The large value of Δh_3^0 for this system can be attributed to its ionic nature. The equilibrium structure of MgO places each ion in an environment in which it is nearest to ions bearing an opposite charge. Meanwhile, the TS aligns ions with like charges on either side of slip interface. The associated Coulomb repulsion leads to a separation of the interface and increase in the thickness of the system.

The results in Fig. 5 also indicate that despite being structurally analogous, covalently bonded materials Si and Ge exhibit vastly different μ_s values of 0.046 and 0.308, respectively. These materials have similar values of ΔE_{slip} and G, leading to similar values of $r_s = 2.2$ and 1.9 Å for Si and Ge, respectively. As such, according to Eq. (20), the differences in μ_s for these systems can be attributed to differences in Δh_3^0 and G'. The data in Table III show that Si has a negative value of Δh_3^0, whereas Ge has a large positive value for this quantity. This difference in Δh_3^0 can be attributed to differences in the stiffnesses of the tetrahedral structures around each atom in these systems. Additionally, Ge has a higher value of G' than Si, which is due to the lower stiffness of Ge along the direction in which L is applied. This is clear from calculations of the component of the stiffnesses matrices C_{33} associated with the direction normal to the slip interface being lower for Ge (7.25 nN Å^{-1}) than it is for Si (9.48 nN Å^{-1}). Collectively, the lower values of Δh_3^0 and G' for Si relative to those of Ge cause μ_s to be lower for Si than it is for Ge.

The lamellar systems considered here undergo a slip process that involves changes in relatively weak nonbonding interactions, e.g., van der Waals interactions or hydrogen bonds. As a result, ΔE_{slip} and G are relatively low for these systems, which lead to low values of F_s, and consequently these systems are used as solid lubricants. However, the values of μ_s span a wide range of values from 0.082 for graphite to 0.245 for WS_2. In what follows, we use Eq. (20) to account for differences or similarities between for distinct sets of structurally analogous layered materials.

MoS_2 and WS_2 are structurally analogous lamellar materials, with each material consisting of sheets containing three atomic layers. For both materials, slip involves the movement of the sheets relative to one another, with nonbonding interactions between the S atoms on neighboring sheets being the primary contributors to the slip barrier. Despite these similarities, μ_s for WS_2 (0.245) is approximately 40% higher than that of MoS_2 (0.170). The origin of this difference is apparent through the application of Eq. (20). Both systems exhibit similar values of ΔE_{slip} and G, and thus r_s^0 is similar for both materials. In addition, both materials possess similar values of G', and hence μ_s is determined primarily by Δh_3^0. The data in Table III show that Δh_3^0 for WS_2 is nearly double that of MoS_2. This difference leads to the larger value of μ_s for WS_2 and is likely due to differences in the electronegativities of Mo and W, which lead to different partial charges on the S atoms in these systems that cause the sheets in WS_2 to separate by a greater degree during slip than those in MoS_2.

Graphite and BN each consist of stacked layers that are one atom thick, with the atoms in each layer arranged hexagonally. Slip occurs as the layers slide past one another. Both materials exhibit similar values of μ_s, with $\mu_s = 0.082$ and 0.089 for graphite and BN, respectively. The similar values of μ_s for these two systems are a result of the similarities of all parameters entering Eq. (20) for these two systems. The similarity in the parameters is likely a result of the slip barrier and F_s being dominated by dispersion interactions for both these system and the similarity of dispersion parameters for B, C, and N.

Finally, graphane, FG, and HFG have similar layered structures and undergo analogous slip mechanisms in which one layer moves past another. The slip process is dominated by nonbonding interactions. The results show that the slip barriers for these materials are arranged as $\Delta E_{\text{slip}}^{0,\text{FG}} < \Delta E_{\text{slip}}^{0,\text{graphane}} < \Delta E_{\text{slip}}^{0,\text{HFG}}$. This order is consistent with the nature of the interactions between the layers in the materials. Specifically, the interlayer interactions in FG are dominated by repulsive Coulomb interactions between F atoms, those in graphane are dominated by slightly attractive van der Waals interactions between H atoms, and those in HFG are dominated by hydrogen bonds. The relative magnitudes of μ_s for these materials does not match the ordering of the slip barriers. Instead, FG and HFG exhibit similar values of μ_s (FG: 0.090, HFG: 0.109), while graphane exhibits a higher μ_s (0.176). The data in Table III indicate that FG and HFG have values of G' that are significantly lower than that of graphane. The low values of G' for FG and HFG cause μ_s for these systems to be dictated primarily by Δh_3^0. Meanwhile, the higher G' for graphane causes both terms in Eq. (20) to contribute to μ_s for this system, leading to a higher friction coefficient. It is somewhat surprising that the strongest (HFG) and weakest (FG) of these three interfaces exhibit similar and low values of G', while the interface of intermediate strength (graphane) exhibits the highest G'. This difference can be understood by examining the nature of the interactions between the surfaces in these systems. In FG, the presence of fluorine atoms bearing partial negative charges leads to repulsive interactions across the interface, which resist changes in structure upon the application of L and cause G' to be low. Similarly, the hydrogen bonding interactions across the interface in HFG also cause this system to resist deformation upon the application of L also leading to low G'. Meanwhile, the relatively weak dispersive interactions between the H atoms present at the surfaces of the graphane layers cause this material to be more compliant to L, leading to a larger value of G'.

Overall, the analyses presented above illustrate how Eq. (20) can be used to relate μ_s to measurable properties of sliding interfaces. This may be useful in the context of interpreting experimental measurements of friction coefficients or

designing interfaces with particular values of μ_s. Moreover, the application of Eq. (20) sheds lights on interesting phenomena related to the manner in which different structural, energetics, and mechanical features of interfaces affect μ_s.

Although it is not the intention of this work to reproduce the experimental friction coefficients, we briefly discuss the ability of the models in predicting the experimental μ_s data. It is well established that molecular simulations can only be used as predictive tools for investigating friction if the model system is carefully designed to be as close as possible to the experimental conditions [60]. This general statement can be also applied to the models presented here. Accordingly, the values of μ_s presented here can be considered as the static friction coefficient at the cryogenic temperatures and in the absence of wear, adsorbed molecules, and surface oxidation layers. Comparison of the friction coefficients calculated from our model with available experimental data obtained at conditions close to those used in this work indicates that the predicted values are within the range of the experimental data [43]. For instance, the values of μ_s obtained from the shear-based model for Si (0.05) and MoS_2 (0.15) are comparable to the experimental values of 0.05 [76] and 0.17 [77], respectively. In addition, this model can capture the experimentally observed dependencies of μ_s on properties such as slip direction and adhesive interactions between surfaces in contacts [78,79].

D. Analysis of the friction coefficient

The shear-based model of μ_s suggests that the friction coefficient is dependent on several, likely interrelated, parameters associated with the system. Minimizing Eq. (20) with respect to Δr_s^0, in conjunction with the assumption that G' and Δh_3^0 are both positive, shows that μ_s reaches a minimum value when

$$\Delta r_s^0 = \sqrt{2\Delta E_{\text{slip}}^0/G} = \sqrt{2\Delta h_3^0/G'}, \tag{21}$$

which leads to a minimum $L = 0$ friction coefficient of

$$\mu_s^{min}(0) = \sqrt{2G'\Delta h_3^0}. \tag{22}$$

Equations (21) and (22) can be useful in the context of developing systems with desired values of μ_s. In particular, Eq. (21) provides the condition that should be satisfied to achieve the lowest value of μ_s possible for an interface. The parameters ΔE_{slip}^0, G, G', and Δh_3^0 are interrelated and thus it may not be possible to alter one of these parameters without affecting the others. Nonetheless, as illustrated in Sec. IV C, it is possible to qualitatively relate the values of these properties to fundamental features of the system such as bond energies, bond stiffnesses, and the geometry of the interface, and to predict how modifications to the system will affect μ_s. In cases where a low μ_s is required, this expression can be used to filter out materials whose values of G' and Δh_3^0 will not permit sufficiently low values of μ_s to be reached. Conversely, in applications requiring high μ_s, this expression can be used to identify interfaces with high values of this quantity.

The development of Eqs. (21) and (22) relied on the assumption that G' and Δh_3^0 are both positive quantities. The assumption that G' is positive should hold for the majority of materials unless the material undergoes a structural change, e.g., a phase transition, upon the application of L that leads to a drastic change in its mechanical properties. However, it is possible to attain a negative value of Δh_3^0 since this quantity simply depends on the structural changes that occur during slip. In principle, negative Δh_3^0 could lead to a negative friction coefficient, which has been observed experimentally [80].

The zero-L limit of μ_s is suitable for most applications, which involve systems that are subjected to changes in loads from a reference value near $L = 0$. Nonetheless, it is worth briefly examining the L-dependent terms in Eq. (19). Note that the numerator in this equation dominates as L is increased, so the role of the load dependence of the numerator in modifying μ_s at higher L will be emphasized in what follows. Equation (19) reveals that μ_s depends on L through the terms $(2G'\Delta h_3^0)L$, $(-G\Delta\chi_{33}^0/2)L$, and $(-3G'\Delta\chi_{33}^0/4)L^2$. The first term, $(2G'\Delta h_3^0)L$, incorporates the L dependence of the shear potential into the increase in F_s required to perform sufficient work on the system to overcome the changes in the thickness during slip in the presence of L. The second term, $(-G\Delta\chi_{33}^0/2)L$, quantifies the increase in F that must occur to overcome the L-dependent changes in ΔE_{slip} and Δh_3^0 assuming that E_{shear} is independent of L. However, $\Delta\chi_{33}^0$ enters this term with a negative sign. As such, positive values of this quantity reduce μ_s. The term designated $(-3G'\Delta\chi_{33}^0/4)L^2$ accounts for the L-dependent changes in ΔE_{slip} and Δh_3 captured by $\Delta\chi_{33}^0$ in conjunction with the L dependence of the curvature of E_{shear}. This term is preceded by a negative sign, so once again positive values of $\Delta\chi_{33}^0$ reduce μ_s.

Overall, the consideration of the L-dependent terms sheds light on the role of $\Delta\chi_{33}^0$ in determining μ_s. In particular, a positive $\Delta\chi_{33}^0$ will reduce μ_s, whereas the opposite is true for negative $\Delta\chi_{33}^0$. A positive $\Delta\chi_{33}^0$ indicates that the TS is more compliant with respect to L than R. The values in Table III indicate that $\Delta\chi_{33}^0$ is small for all systems considered in this work and can adopt positive or negative values. Positive values are attained for systems like Si and Ge, where covalent bonds are broken as the system moves passed the TS, which presumably decreases the ability of the TS to support L relative to R. Meanwhile, negative values of $\Delta\chi_{33}^0$ are found for most systems in which slip involves changes in nonbonded interactions, e.g., BN and graphite. In these systems, slip involves atoms on either side of the slip plane becoming aligned in the TS. This alignment increases the repulsion between the layers and causes the system to become stiffer normal to the slip plane in the TS than in R. While only a limited set of systems have been examined here, the data suggest that the terms related to $\Delta\chi_{33}^0$ may cause μ_s to decrease with increasing L for covalently bonded interfaces and increase for systems that are dominated by dispersion interactions. It should be noted that for these systems investigated here, the magnitudes of $\Delta\chi_{33}^0$ are very small in all cases and thus such effects only likely become apparent at high loads.

V. CONCLUSIONS

In this study, we have developed and investigated models for relating the friction coefficient to material properties. The models consider a slip process as an activated transition between two energetically stable structures connected by a transition state. The dependence of the slip energy barrier on load is

obtained via second-order Taylor series expansions of the energies of the reactant and transition state structures with respect to load. The resulting expression for the slip energy barrier is used in conjunction with the Prandtl-Tomlinson model and a model based on shear energies. The abilities of both models to predict friction forces F_f and static friction coefficients μ_s in the low-T limit for a wide range of materials with ionic, covalent, and nonbonding interactions were assessed with respect to first-principles molecular dynamics simulations. The results indicate that although both the Prandtl-Tomlinson and the shear-based models reproduce the F_f values obtained from FPMD simulations with comparable accuracies, but the shear-based model has a better performance in predicting the reference μ_s data. This model also provides quantitative information about the contribution of various well-defined material and contact properties in the friction coefficient. All such parameters can be obtained from DFT calculations. Performing quantitative analyses of the friction coefficients obtained for the systems investigated here reveals that the structural changes of material during the slip event, along with the energetic terms, might have an important contribution in the magnitude of μ_s. The model also explains the origin of the differences in friction coefficients obtained for systems with similar structures. Such information might be very useful in improving the efficiency of solid lubricants and sliding contacts.

Overall, this work illustrates that the friction coefficient can be described in terms of a model that relates this quantity to basic energetic, structural, and mechanical properties of the contact. The model presented here can be used to explain the atomistic origin of the friction coefficient, rationalize differences in the values of the friction coefficient for different materials, and can also provide guidance for altering it in the context of materials' design. The information provided by the model can be also used to explain the results of molecular simulations and experimental investigations in light of mechanical and interface properties of materials. We have also shown that the model can be augmented with appropriate terms to include the effect of temperature, velocity, and contact area. Quantitative investigation of such effects and also comprehensive application of the model for explaining the factors affecting the friction coefficient in systems with technological importance will be the subject of our future works. The results presented here are expected to inspire further experimental and computational investigations to rationalize the relation between the friction coefficient and material properties in order to shed light on the atomistic origin of the friction coefficient.

ACKNOWLEDGMENTS

Financial support from the Natural Sciences and Engineering Research Council (NSERC) of Canada Discovery Grant Program and the Ontario Ministry of Research and Innovation is gratefully acknowledged. Computing resources were provided by Compute Canada.

[1] S. Chu and A. Majumdar, Nature (London) **488**, 294 (2012).
[2] K. Holmberg, P. Andersson, and A. Erdemir, Tribol. Int. **47**, 221 (2012).
[3] H. P. Jost, Tribol. Lubr. Technol. **61**, 18 (2005).
[4] B. Bhushan, J. Israelachvili, and U. Landman, Nature (London) **374**, 607 (1995).
[5] M. Urbakh, J. Klafter, D. Gourdon, and J. Israelachvili, Nature (London) **430**, 525 (2004).
[6] M. Marder, Nat. Mater. **3**, 583 (2004).
[7] J. Frenken, Nat. Nanotechnol. **1**, 20 (2006).
[8] E. Meyer, Science **348**, 1089 (2015).
[9] K. M. Liechti, Science **348**, 632 (2015).
[10] S. Zapperi, Science **330**, 184 (2010).
[11] M. Urbakh and E. Meyer, Nat. Mater. **9**, 8 (2010).
[12] A. Bylinskii, D. Gangloff, and V. Vuletic, Science **348**, 1115 (2015).
[13] J. Y. Park, D. F. Ogletree, M. Salmeron, R. A. Ribeiro, P. C. Canfield, C. J. Jenks, and P. A. Thiel, Science **309**, 1354 (2005).
[14] E. Koren, E. Loertscher, C. Rawlings, A. W. Knoll, and U. Duerig, Science **348**, 679 (2015).
[15] C. J. Carkner, S. M. Haw, and N. J. Mosey, Phys. Rev. Lett. **105**, 056102 (2010).
[16] Q. Li, X.-Z. Liu, S.-P. Kim, V. B. Shenoy, P. E. Sheehan, J. T. Robinson, and R. W. Carpick, Nano Lett. **14**, 5212 (2014).
[17] R. J. Cannara, M. J. Brukman, K. Cimatu, A. V. Sumant, S. Baldelli, and R. W. Carpick, Science **318**, 780 (2007).
[18] A. Socoliuc, E. Gnecco, S. Maier, O. Pfeiffer, A. Baratoff, R. Bennewitz, and E. Meyer, Science **313**, 207 (2006).
[19] L. Prandtl, Z. Angew. Math. Mech. **8**, 85 (1928).
[20] G. A. Tomlinson, Philos. Mag. **7**, 905 (1929).
[21] H. Spikes and W. Tysoe, Tribol. Lett. **59**, 1 (2015).
[22] S. Y. Krylov and J. W. M. Frenken, Phys. Status Solidi B **251**, 711 (2014).
[23] A. Vanossi, N. Manini, M. Urbakh, S. Zapperi, and E. Tosatti, Rev. Mod. Phys. **85**, 529 (2013).
[24] V. L. Popov and J. A. T. Gray, Z. Angew. Math. Mech. **92**, 683 (2012).
[25] Y. Dong, A. Vadakkepatt, and A. Martini, Tribol. Lett. **44**, 367 (2011).
[26] T. Gyalog, E. Gnecco, and E. Meyer, *NanoScience and Technology* (Springer, Berlin, 2007), p. 101.
[27] E. Gnecco, R. Bennewitz, T. Gyalog, C. Loppacher, M. Bammerlin, E. Meyer, and H.-J. Guntherodt, Phys. Rev. Lett. **84**, 1172 (2000).
[28] Y. Sang, M. Dube, and M. Grant, Phys. Rev. Lett. **87**, 174301 (2001).
[29] E. Riedo, E. Gnecco, R. Bennewitz, E. Meyer, and H. Brune, Phys. Rev. Lett. **91**, 084502 (2003).
[30] A. Socoliuc, R. Bennewitz, E. Gnecco, and E. Meyer, Phys. Rev. Lett. **92**, 134301 (2004).
[31] Z. Tshiprut, S. Zelner, and M. Urbakh, Phys. Rev. Lett. **102**, 136102 (2009).
[32] L. Jansen, H. Holscher, H. Fuchs, and A. Schirmeisen, Phys. Rev. Lett. **104**, 256101 (2010).

[33] M. H. Muser, Phys. Rev. B **84**, 125419 (2011).
[34] O. J. Furlong, S. J. Manzi, V. D. Pereyra, V. Bustos, and W. T. Tysoe, Tribol. Lett. **39**, 177 (2010).
[35] D. Perez, Y. Dong, A. Martini, and A. F. Voter, Phys. Rev. B **81**, 245415 (2010).
[36] O. J. Furlong, S. J. Manzi, V. D. Pereyra, V. Bustos, and W. T. Tysoe, Phys. Rev. B **80**, 153408 (2009).
[37] G. Amontons, *Memoires de l'Academie Royale A* (1699), p. 257.
[38] P. Heilmann and D. Rigney, Wear **72**, 195 (1981).
[39] J. Ogilvy, J. Phys. D: Appl. Phys. **24**, 2098 (1991).
[40] J. Zhang, F. Moslehy, and S. Rice, Wear **149**, 1 (1991).
[41] S. M. Hsu and Z. C. Ying, *Nanotribology: Critical Assessment and Research Needs* (Kluwer Academic, New York, 2003).
[42] R. Maboudian and C. Carraro, Annu. Rev. Phys. Chem. **55**, 35 (2004).
[43] A. Erdemir, *Modern Tribology Handbook* (CRC Press, Boca Raton, FL, 2001).
[44] T. W. Scharf and S. V. Prasad, J. Mater. Sci. **48**, 511 (2013).
[45] W. Zhong and D. Tomanek, Phys. Rev. Lett. **64**, 3054 (1990).
[46] M. Weiss and F.-J. Elmer, Phys. Rev. B **53**, 7539 (1996).
[47] T. Gyalog and H. Thomas, Europhys. Lett. **37**, 195 (1997).
[48] H. Hölscher, A. Schirmeisen, and U. D. Schwarz, Phil. Trans. R. Soc. A **366**, 1383 (2008).
[49] N. L. McCook, D. L. Burris, P. L. Dickrell, and W. G. Sawyer, Tribol. Lett. **20**, 109 (2005).
[50] A. Schirmeisen, L. Jansen, H. Hlscher, and H. Fuchs, Appl. Phys. Lett. **88**, 123108 (2006).
[51] J. C. Burton, P. Taborek, and J. E. Rutledge, Tribol. Lett. **23**, 131 (2006).
[52] X. Zhao, M. Hamilton, W. G. Sawyer, and S. S. Perry, Tribol. Lett. **27**, 113 (2007).
[53] M. A. Hamilton, L. A. Alvarez, N. A. Mauntler, N. Argibay, R. Colbert, D. L. Burris, C. Muratore, A. A. Voevodin, S. S. Perry, and W. G. Sawyer, Tribol. Lett. **32**, 91 (2008).
[54] X. Zhao, S. R. Phillpot, W. G. Sawyer, S. B. Sinnott, and S. S. Perry, Phys. Rev. Lett. **102**, 186102 (2009).
[55] C. Marone, Annu. Rev. Earth Planet. Sci. **26**, 643 (1998).
[56] M. H. Muser, Proc. Natl. Acad. Sci. USA **105**, 13187 (2008).
[57] Z. Yang, H. P. Zhang, and M. Marder, Proc. Natl. Acad. Sci. USA **105**, 13264 (2008).
[58] T. Kontorova and Y. I. Frenkel, Zh. Eksp. Teor. Fiz. **8**, 1340 (1938).
[59] N. J. Mosey and E. A. Carter, J. Mech. Phys. Solids **57**, 287 (2009).
[60] Y. Dong, Q. Li, and A. Martini, J. Vac. Sci. Technol. A **31**, 030801 (2013).
[61] X.-Z. Liu, Z. Ye, Y. Dong, P. Egberts, R. W. Carpick, and A. Martini, Phys. Rev. Lett. **114**, 146102 (2015).
[62] R. W. G. Wyckoff, *Crystal Structures* (Interscience, New York, 1963).
[63] D. C. Elias, R. R. Nair, T. M. G. Mohiuddin, S. V. Morozov, P. Blake, M. P. Halsall, A. C. Ferrari, D. W. Boukhvalov, M. I. Katsnelson, A. K. Geim, and K. S. Novoselov, Science **323**, 610 (2009).
[64] S.-H. Cheng, K. Zou, F. Okino, H. R. Gutierrez, A. Gupta, N. Shen, P. C. Eklund, J. O. Sofo, and J. Zhu, Phys. Rev. B **81**, 205435 (2010).
[65] P. Hohenberg and W. Kohn, Phys. Rev. **136**, B864 (1964).
[66] W. Kohn and L. J. Sham, Phys. Rev. **140**, A1133 (1965).
[67] J. P. Perdew, K. Burke, and M. Ernzerhof, Phys. Rev. Lett. **77**, 3865 (1996).
[68] S. Grimme, J. Comput. Chem. **27**, 1787 (2006).
[69] S. Grimme, J. Antony, S. Ehrlich, and H. Krieg, J. Chem. Phys. **132**, 154104 (2010).
[70] P. E. Blochl, Phys. Rev. B **50**, 17953 (1994).
[71] D. Sheppard, P. Xiao, W. Chemelewski, D. D. Johnson, and G. Henkelman, J. Chem. Phys. **136**, 074103 (2012).
[72] P. Giannozzi, S. Baroni, N. Bonini, M. Calandra, R. Car, C. Cavazzoni, D. Ceresoli, G. L. Chiarotti, M. Cococcioni, I. Dabo, A. Dal Corso, S. de Gironcoli, S. Fabris, G. Fratesi, R. Gebauer, U. Gerstmann, C. Gougoussis, A. Kokalj, M. Lazzeri, L. Martin-Samos, N. Marzari, F. Mauri, R. Mazzarello, S. Paolini, A. Pasquarello, L. Paulatto, C. Sbraccia, S. Scandolo, G. Sclauzero, A. P. Seitsonen, A. Smogunov, P. Umari, and R. M. Wentzcovitch, J. Phys.: Condens. Matter **21**, 395502 (2009).
[73] M. Parrinello and A. Rahman, J. Appl. Phys. **52**, 7182 (1981).
[74] A. Lees and S. Edwards, J. Phys. C: Solid State Phys. **5**, 1921 (1972).
[75] M. Bernasconi, G. Chiarotti, P. Focher, S. Scandolo, E. Tosatti, and M. Parrinello, J. Phys. Chem. Solids **56**, 501 (1995).
[76] B. Bhushan and X. D. Li, J. Mater. Res. **12**, 54 (1997).
[77] F. J. Clauss, *Solid Lubricants and Self-Lubricating Solids* (Academic, New York, 1972).
[78] A. J. Weymouth, D. Meuer, P. Mutombo, T. Wutscher, M. Ondracek, P. Jelinek, and F. J. Giessibl, Phys. Rev. Lett. **111**, 126103 (2013).
[79] J. P. Gao, W. D. Luedtke, D. Gourdon, M. Ruths, J. N. Israelachvili, and U. Landman, J. Phys. Chem. B **108**, 3410 (2004).
[80] Z. Deng, A. Smolyanitsky, Q. Li , X.-Q. Feng, and R. J. Cannara, Nat. Mater. **11**, 1032 (2012).